

The Bimodal Distribution in Exoplanet Radii: Considering Varying Core Compositions and H₂ Envelop Sizes

DARIUS MODIRROUSTA-GALIAN,^{1,2} DANIELE LOCCI,¹ AND GIUSEPPINA MICELA¹

¹*INAF Osservatorio Astronomico di Palermo, Piazza del Parlamento 1, I-90134 Palermo, Italy*

²*University of Palermo, Department of Physics and Chemistry, Via Archirafi 36, Palermo, Italy*

Submitted to APJ

ABSTRACT

Several models have been introduced in order to explain the radius distribution in exoplanet radii observed by [Fulton et al. \(2017\)](#) with one peak at $\sim 1.3R_{\oplus}$ the other at $\sim 2.4R_{\oplus}$ and the minimum at $\sim 1.75R_{\oplus}$. In this paper we focus on the hypothesis that the exoplanet size distribution is caused by stellar XUV-induced atmospheric loss. We evolve 10^6 synthetic exoplanets by exposing them to XUV irradiation from synthetic ZAMS stars. For each planet we set a different interior composition which ranged from 100 wt% Fe (very dense) through 100 wt% MgSiO₃ (average density) and to 100 wt% H₂O ice (low density) with varying hydrogen envelop sizes which varied from 0 wt% (a negligible envelop) to 100 wt% (a negligible core). Our simulations were able to replicate the bimodal distribution in exoplanet radii. We argue that in order to reproduce the distribution by [Fulton et al. \(2017\)](#) it is mandatory for there to be a paucity of exoplanets with masses above $\sim 8M_{\oplus}$. Furthermore, our best-fit result predicts an initial flat distribution in exoplanet occurrence for $M_P \lesssim 8M_{\oplus}$ with a strong deficiency for planets with $\lesssim 3M_{\oplus}$. Our results are consistent with the $\sim 1.3R_{\oplus}$ radius peak mostly encompassing denuded exoplanets whilst the $\sim 2.4R_{\oplus}$ radius peak mainly comprising exoplanets with large hydrogen envelopes.

Keywords: planets and satellites: atmospheres — planets and satellites: terrestrial planets — planet-star interactions — planets and satellites: physical evolution

1. INTRODUCTION

Ever since the discovery of the bimodal distribution in exoplanet sizes ([Fulton et al. 2017](#)) with one peak at $\sim 1.3R_{\oplus}$, the other at $\sim 2.4R_{\oplus}$, and the minimum at $\sim 1.75R_{\oplus}$, multiple models have been put forward attempting to explain this shape. Although formational mechanisms and arguments have been proposed (e.g. [Ginzburg et al. 2016](#); [Gupta & Schlichting 2018](#); [Ginzburg et al. 2018](#); [Zeng et al. 2018](#)), in this paper we will focus on how stellar XUV irradiation erodes away the primordial H₂ – dominated atmospheres of exoplanets (e.g. [Lecavelier Des Etangs 2007](#); [Ehrenreich & Désert 2011](#); [Lammer et al. 2013](#); [Jin et al. 2014](#); [Jin & Mordasini 2018](#); [Kubyshkina et al. 2018a](#)) and its contribution in shaping the distribution. One of the most highly cited models is [Owen & Wu \(2013, 2017\)](#) which assumes that Kepler planets orbiting Sun-like stars, have Earth-like interiors, and have masses that vary according to a Rayleigh distribution with a mode at $\sim 3M_{\oplus}$. According to their model, exoplanets with masses above $\sim 3M_{\oplus}$ had large H₂ atmospheres whilst planets with masses beneath this threshold were born approximately bare. In this paper we take a different and more general approach to atmospheric mass-loss than [Owen & Wu \(2013, 2017\)](#). Specifically, we account for interiors that range from 100 wt% Fe - 100 wt% H₂O that host H₂ envelopes. These primordial envelopes will scale from 0 wt% (a negligible or non-existent atmosphere) to 100 wt% (a negligible or non-existent core) of the total mass. We also do not focus on the process through which an exoplanet loses its atmosphere, just the beginning and

Table 1. Stellar spectral type frequency for known exoplanets with orbital periods ≤ 100 days. Data from the *NASA Exoplanet Archive*.

Type	Number	Norm. Fraction (%)
M	14	0.654
K	376	17.554
G	1311	61.204
F (F5-F9)	441	20.588

Table 2. The properties of our synthetic population [Siess et al. \(2000\)](#).

Type	Mass (M_*)	Radius (R_*)	Temperature (K)
M6	0.1	0.192	2973
M5	0.2	0.224	3244
M3	0.3	0.299	3474
M2	0.4	0.360	3654
M1	0.5	0.430	3811
M0	0.6	0.517	3982
K6	0.7	0.623	4261
K4	0.8	0.735	4617
K2	0.9	0.850	4925
K1	1.0	0.965	5239
G9	1.1	1.110	5475
G7	1.2	1.290	5685
G2	1.3	1.450	5917
F9	1.4	1.640	6116
F7	1.5	1.840	6296
F5	1.6	2.030	6489

the end result. By considering the multiplicity of compositions and envelopes we evolve a synthetic population of 10^6 exoplanets to test whether the bimodal distribution observed by [Fulton et al. \(2017\)](#) could be reproduced.

2. INITIAL CONDITIONS

2.1. Stellar Population

As of September 2019 there are ~ 4000 known exoplanets in total, however for this study we are only interested in the Kepler candidates. To keep in line with [Fulton et al. \(2017\)](#) we only considered planets with orbital periods ≤ 100 days. From these we could extract useful stellar information out of 2171 via the *NASA Exoplanet Archive*. Discarding O-, A-, B- and F0-F5 type stars (which were only 29 in number) left us with 2142. The resultant distribution of stellar spectral types is shown in table 1.

Even if this data set is biased due to instrumental limitations, it was used to generate the bimodal distribution by [Fulton et al. \(2017\)](#), so we may use it to generate a synthetic population of 10^6 ZAMS stars with their spectral-type distribution corresponding to table 1 and their masses, radii and temperatures matching those predicted by [Siess et al. \(2000\)](#). We are aware that stars evolve with age but since most of the XUV-induced evaporation occurs within the first ~ 1 Gyr we can ignore this evolution and instead focus on the irradiation present during the star's youth. We also did not account for small variations within each spectral class of mass, radius, metallicity and temperature since the effects on our final results would be negligible.

In order to estimate the frequency of each sub-type we divided the frequency of each spectral class by the number of sub-types given by [Siess et al. \(2000\)](#). Regarding the XUV stellar irradiation, we used the equations by [Penz & Micela \(2008\)](#) for M-type stars and [Penz et al. \(2008\)](#) for G-type stars with the UV fluxes from [Sanz-Forcada et al. \(2011\)](#). Since K-type stars are intermediate in X-ray luminosity levels we set their values as being in-between M- and

G-types. For late F-type stars we set their XUV luminosities as equivalent to G0-type stars which is adequate for our statistical model.

2.2. Orbital Parameters

When we plot the planetary radii versus the semi-major axis distances, a deficit of bodies intermediate in size between a super-Earth and a sub-Jupiter with short orbital periods (see figure 1) can be seen. This paucity is believed to be due to the photoevaporation of primordial atmospheres (e.g. Owen & Lai 2018). Since our code will evolve synthetic exoplanets from before the time that their atmospheres were eroded, we will assume that there was no gap straight after their formation so a planet with an arbitrary radius could have any arbitrary orbital distance. Notwithstanding, we set an upper limit for the radius of our synthetic exoplanets at $R_P \approx 8.0R_\oplus$ (i.e. $M \approx 25M_\oplus$ for a cold H_2 body) in order to exclude Saturn- and Jupiter-mass planets which are more resilient to atmospheric erosion. With this assumption it became possible to begin sampling exoplanetary orbital distances. The histogram of the semi-major axial distances showed that the average orbit is at ~ 0.1 AU (see figure 2). This distribution was best fit by a lognormal curve between a minimum distance set by the *Roche limit* (Aggarwal & Oberbeck 1974) of each individual star and a maximum distance corresponding to a period of 100 days. We approximated the *Roche limits* of the stars as $\sim 2R_*$, where R_* is the radius of the host star being considered at that moment, because planets with large H_2 envelopes such as the outer planets in our solar system have stellar-like densities. This approximation breaks down for exoplanets born with very small atmospheres but these should be scarce since most planets are thought to begin with large H_2 repositories (e.g. Hayashi et al. 1985; Ikoma & Hori 2012).

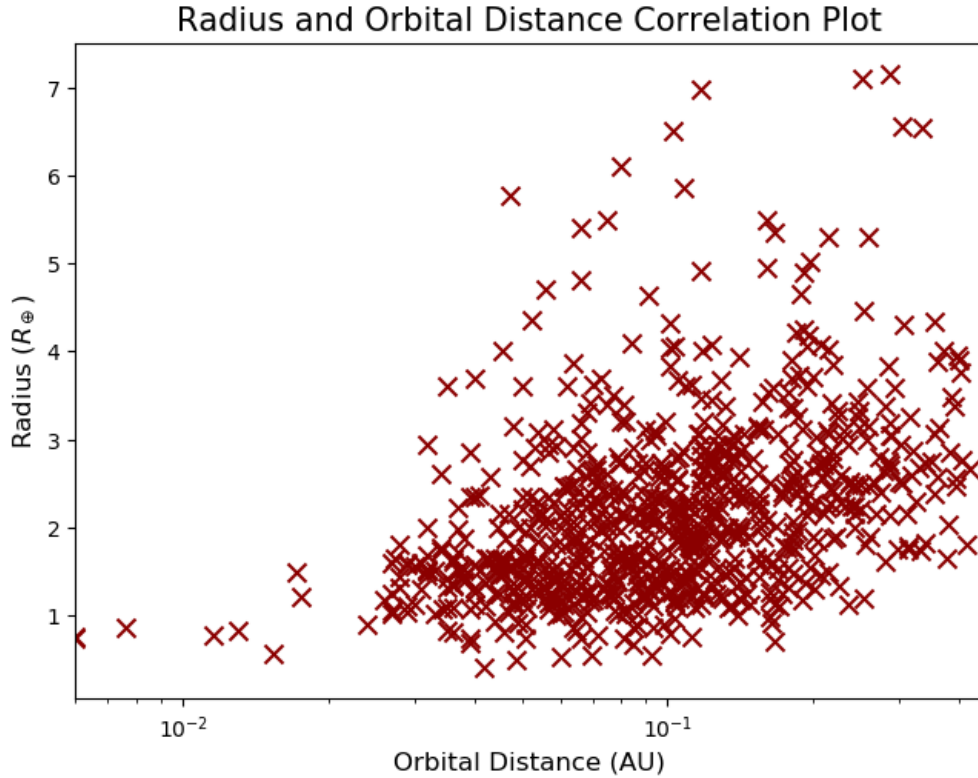


Figure 1. Semi-major axial distance (AU) plotted against planetary radius (R_\oplus) for orbital periods ≤ 100 days. 787 data points all of which were collected on September 2019 from the *NASA Exoplanet Archive*.

2.3. Planetary Parameters

Our initial population of exoplanets was modelled as having H_2 atmospheres so their average densities had to be lower than a purely silicate planet. However, it is possible that some exoplanets formed with very small or non-existent atmospheres whilst others formed almost entirely as hydrogen spheres with no core. Consequently we modelled the

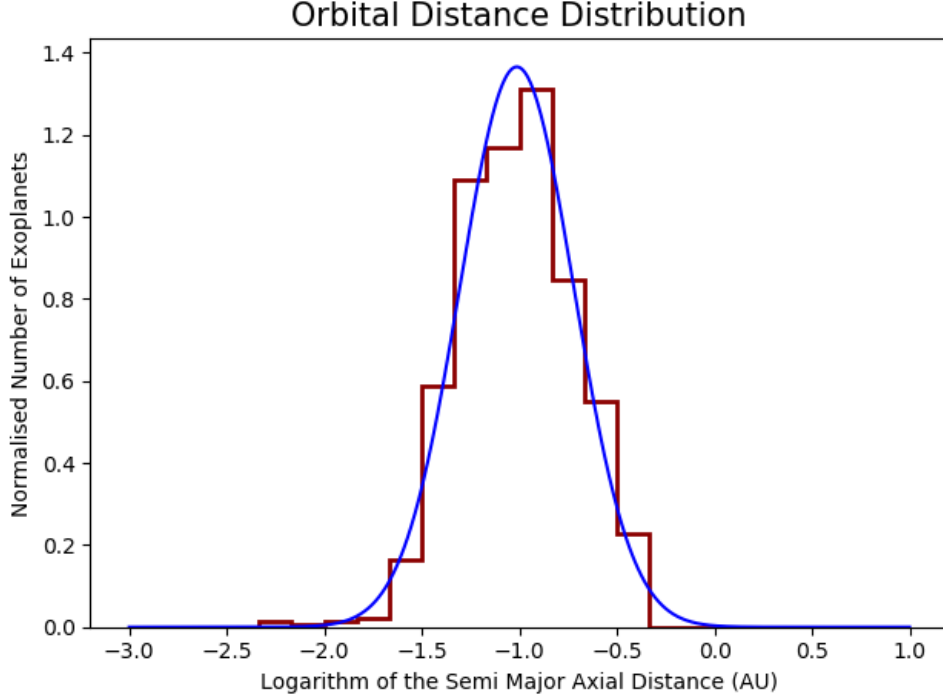


Figure 2. The normalised observed distribution of exoplanet orbital distances (red) and the lognormal approximation (blue) for exoplanets with orbital periods ≤ 100 days. 838 data points all of which were collected on September 2019 from the *NASA Exoplanet Archive*.

variation in exoplanet radii with a laplace distribution were for each planet the maximum allowed density was set as a 100 wt% Fe sphere, the minimum density was modelled as a 100 wt% H₂ sphere, and the average density was given by a terran core with a H₂-rich atmosphere. For the Fe and terran mass-radius models we approximated the numerical data in Zeng & Sasselov (2013) and Zeng et al. (2016) with a best-fit curve whilst for the pure hydrogen planet we used Becker et al. (2014). Figure 3 shows the mass and radius relation of 500 synthetic exoplanets as given by our laplace distribution.

100 wt% Fe planet radius (Zeng & Sasselov 2013; Zeng et al. 2016):

$$\frac{R_{Fe}}{R_{\oplus}} = 0.815 \times \left(\frac{M_P}{M_{\oplus}} \right)^{1/4.176} \quad (1a)$$

Terran planet with ~ 1 wt% H₂-rich envelop radius (Zeng & Sasselov 2013; Zeng et al. 2016):

$$\frac{R_{Rock+H_2}}{R_{\oplus}} = 1.410 \times \left(\frac{M_P}{M_{\oplus}} \right)^{1/3.905} \quad (1b)$$

100 wt% H₂ planet radius (Becker et al. 2014; Zeng et al. 2018):

$$\frac{R_{H_2}}{R_{\oplus}} = 4.106 \times \left(\frac{M_P}{M_{\oplus}} \right)^{1/5.010} \quad (1c)$$

Where M_P is the planetary mass in kg, M_{\oplus} is Earth's mass in kg, and R_{\oplus} is Earth's radius in m. Regarding the planetary mass, we have very few measurements for super-Earths and sub-Neptunes, and even when we do have values they sometimes suffer from large uncertainties. Because of this, we have very strong observational biases towards larger masses (e.g. Howard et al. 2010; Marcy et al. 2014; Malhotra 2015) which means that as of now it is not possible to accurately and reliably know the mass function of exoplanets. Consequently, we will set the initial planetary mass

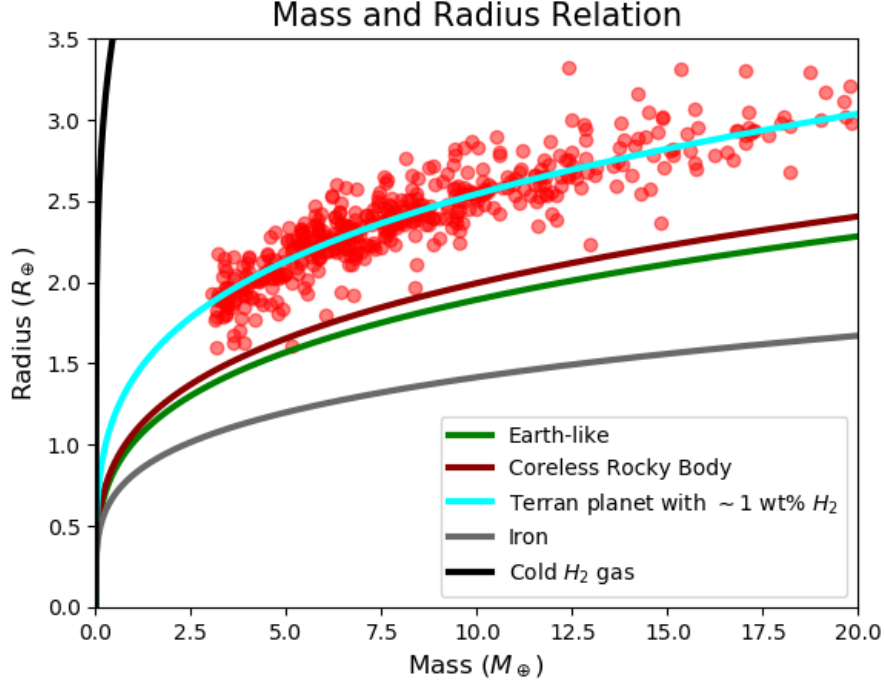


Figure 3. The mass and radius distribution of 500 of our synthetic exoplanets before undergoing photoevaporation. All mass and radius curves come from Zeng & Sasselov (2013) and Zeng et al. (2016) except for the cold H_2 curve which originated from the equations of state by Becker et al. (2014) that were then adapted by Zeng et al. (2018). The radius distribution was given by a laplacian function with a mean corresponding to a terran planet with 1 wt% H_2 envelop and a scale parameter of 0.10 (i.e. a standard deviation of $\sqrt{2}/10$). The reason for the lack of planets with $M_P < 3M_\oplus$ is explained later in the manuscript.

distribution as a variable which we will manually adjust in order match the observed radius gap as given by Fulton et al. (2017).

Some planets are young enough that their atmospheres are still extant despite strong irradiation that would, in the future, denude the planet. These bodies are younger than the amount of time required for their complete atmospheric loss. Using the age of their host stars which is given by the *NASA Exoplanet Archive* as proxies, the age distribution of exoplanets is best described by a truncated gaussian with a mean of ~ 2.9 Gyr, standard deviation of ~ 4.3 Gyr and a minimum and maximum age of ~ 0.25 Gyr and ~ 13.5 Gyr respectively (shown in Figure 4). It is important to note that the age of the stars cannot be directly measured and it is calculated using theoretical modelling which is known to be uncertain. However, it is beyond the scope of this study to do an in-depth analysis of these models. With regards to the mass-loss timescale, for a super-Earth or sub-Neptune this is approximated by:

$$t_{mass\ loss} \sim \frac{M_{env}}{\dot{M}_{env}} \quad (2a)$$

Where

$$M_{env} = \begin{cases} 0.01M_P & \text{if } M_P < \Upsilon_\alpha \\ M_P - \Gamma_\beta & \text{if } \Upsilon_\alpha \leq M_P < \Upsilon_\beta \\ M_P - \Gamma_\gamma & \text{if } M_P \geq \Upsilon_\beta \end{cases} \quad (2b)$$

Where M_{env} is the mass of the primordial envelop, \dot{M}_{env} is the hydro-based mass-loss rate which is described in Kubyshkina et al. (2018b). Since in our study we only focused on the beginning and end result of the mass-loss evolution, we could not include the time dependence on the XUV flux rate. Therefore, in order not to make an overestimation (e.g. by assuming a constant initial flux throughout the lifetime of the star), we modelled this parameter as a step function where $F_{XUV} = F_0$ from 0 – 1 Gyrs and $F_{XUV} = 0$ for > 1 Gyrs. The initial flux F_0 was adopted from (Penz & Micela 2008; Penz et al. 2008; Sanz-Forcada et al. 2011). In addition, the treatment of the

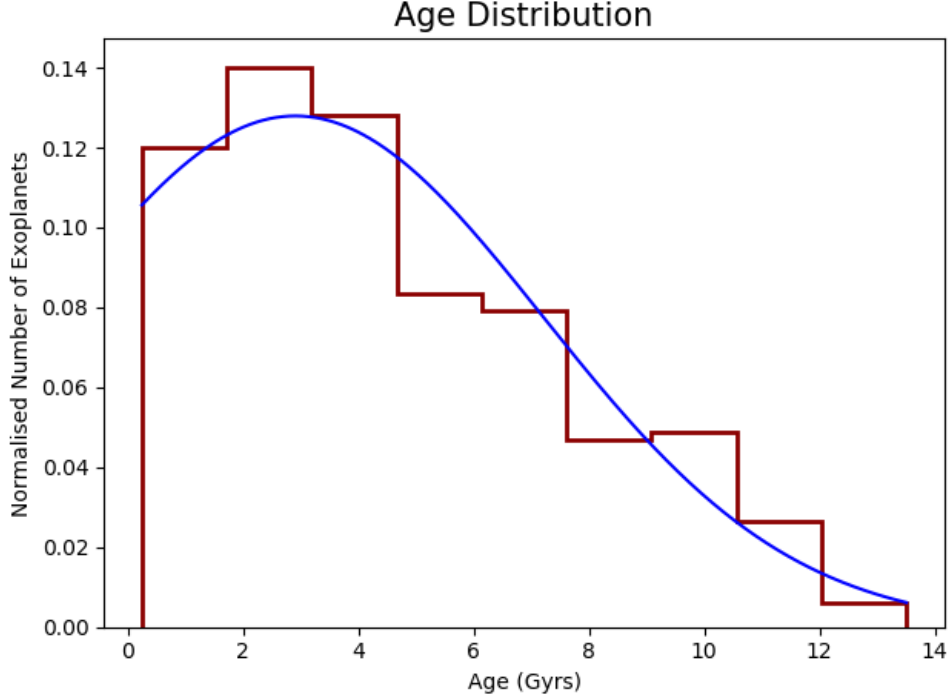


Figure 4. The observed normalised distribution of exoplanet ages (red) and the truncated gaussian approximation (blue) for orbital periods ≤ 100 days. All 341 data points were collected on September 2019 from the *NASA Exoplanet Archive*. We only used Kepler candidates.

flux as a step function is consistent with these studies as during the first billion years of a stars' life the XUV flux is approximately constant, with it then quickly decaying by several orders of magnitude. In the appendix we present Figures (14,15) which show that this approximation is adequate. Regarding Υ_α and Υ_β , these are the critical masses that separate the different regimes α , β and γ . Γ_β and Γ_γ are probabilistic functions with ranges between $\Upsilon_\alpha - M_P$ and $\Upsilon_\beta - M_P$ respectively. When Γ_β or $\Gamma_\gamma = M_P$ this implies that the planetary envelop is nonexistent, whilst if $\Gamma_\beta = \Upsilon_\alpha$ or $\Gamma_\gamma = \Upsilon_\beta$ are for the cases when the planet has the minimum core mass required to be in that specific region:

1. α marks the region where smaller planets typically accrete hydrogen envelopes that are $\sim 1\%$ of the total planetary mass (e.g. [Stevenson 1999](#); [Ikoma & Hori 2012](#); [Chachan & Stevenson 2018](#)). This region will be within the mass limits of $0 - \Upsilon_\alpha$.
2. β is where planets have enough mass to accrete larger envelopes but the cores are still not massive enough to form Neptunian- or Jupiter-mass bodies (e.g. [Ikoma & Hori 2012](#); [Chachan & Stevenson 2018](#)). Region β will be within the mass limits of Υ_α and Υ_β .
3. In the γ region planets undergo runaway gas accretion. This implies that generally any extra mass above the critical mass Υ_β will mostly be due to hydrogen gas. Generally theoretical models predict that the critical mass $\Upsilon_\beta \sim 10M_\oplus$ (e.g. [Ida & Lin 2004, 2005, 2008](#); [Mordasini et al. 2009](#)). However, as systems undergo runaway growth planetesimals are also accreted which could increase the mass of the core ([Shiraishi & Ida 2008](#); [Shibata & Ikoma 2019](#)). This extra growth of the core needs to be balanced with the core erosion induced from deposited energy but the latter effect is believed to be inefficient ([Moll et al. 2017](#)). In addition, internal models of the gaseous planets in our solar system predict core masses in the range of $7 - 25M_\oplus$ (e.g. [Mizuno 1980](#); [Stevenson 1982](#); [Hubbard & Marley 1989](#); [Chabrier et al. 1992](#); [Guillot et al. 1997](#); [Gudkova & Zharkov 1999](#); [Guillot 1999](#); [Wahl et al. 2017](#)). Therefore the remnant cores of Neptunian or Jovian planets could be $> 10M_\oplus$. The possibility of very heavy cores is also supported by the discovery of rocky mega-Earths such as BD+20 594 b which has a mass and radius of $16.3 \pm 6.0M_\oplus$ and $2.2 \pm 0.1R_\oplus$ ([Espinoza et al. 2016](#)) or K2-66 b with $21.3 \pm 3.6M_\oplus$ and $2.50 \pm 0.3R_\oplus$ ([Sinukoff et al. 2017](#)) respectively. Therefore whilst the critical mass $\Upsilon_\beta \sim 10M_\oplus$, the probabilistic function Γ_γ could range from $10 - 25M_\oplus$ according to observations and theoretical predictions.

Having considered all of the above, we will adjust our input distributions for Γ_β and Γ_γ and our critical masses Υ_α and Υ_β in order to find a best fit radius distribution.

3. EVOLUTION MODEL

The simplest summary of our model is that our synthetic exoplanets travel one of three evolutionary paths:

1. The exoplanet is younger than its mass-loss timescale so it currently maintains its envelop.
2. The exoplanet has the right orbital and physical properties required for its primordial envelop to outlive its host star's lifetime (Locci et al. 2019).
3. The exoplanet loses its atmosphere before undergoing any counter-mechanism.

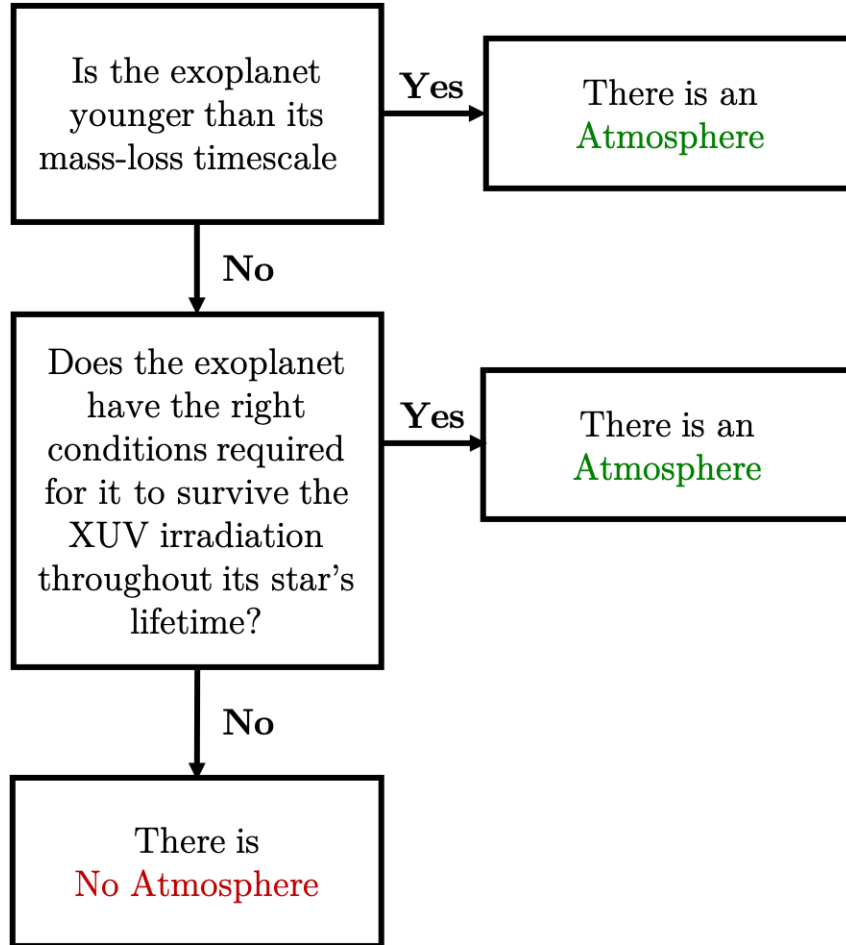


Figure 5. Flowchart showing the path our code took when evolving the exoplanets.

In our code we integrated an algorithm (see figure 5) which implemented the above points. Now that we knew each evolutionary path, we needed to model each step accordingly.

3.1. First Path

If the age of the planet is less than the mass loss timescale we did not evolve it (see equation 3). However, if the contrary is true we moved it to the next stage.

$$t_{age} < t_{mass\ loss} \quad (3)$$

3.2. Second Path

The second path is concerned with whether the initial mass of an exoplanet’s envelop is large enough to survive the incident XUV irradiation for the remainder of the host stars life. In order to estimate this minimum survivable mass, we first calculated the mass loss rate for different synthetic giant exoplanets. To do this we adapted the numerical model for the mass loss rate described in [Locci et al. \(2019\)](#). This model calculates the mass loss rate using the energy-limited approach which was first proposed by [Watson et al. \(1981\)](#) and was later revisited by [Erkaev et al. \(2007\)](#). We then performed a temporal evolution of the synthetic gaseous planet population, where at each arbitrary unit of time we:

1. Calculated the mass loss rate.
2. Updated the total planetary mass.
3. Updated the planetary radius accounting for both: mass lost and gravitational shrinking (see [Locci et al. 2019](#), for details).

For the duration of the simulation we adopted:

- An average G-type lifetime of 10 Gyrs.
- Different possible exoplanet orbital distances.
- Varying initial X-ray luminosities of the parent star.

After the evolution we took note of the planets that ended up as super-Earths from which we then retrieved their initial masses for their given distances and stellar X-ray luminosities. When a planet ended its evolution with a mass less than $2.6M_{\oplus}$, we defined it as having lost all of its gaseous envelope. We chose $2.6M_{\oplus}$ as according to the mass-radius relations of [Zeng & Sasselov \(2013\)](#) and [Zeng et al. \(2016\)](#) this would correspond to a rocky planet with a radius at $\sim 1.3R_{\oplus}$ which according to [Fulton et al. \(2017\)](#) is located at the first peak of the radius distribution. If the planet instead has a hydrogen envelop with a total combined mass of $2.6M_{\oplus}$, its radius would be $\sim 1.8R_{\oplus}$ which is located within the Fulton gap. Consequently, this mass threshold implies that planets originally located within the region of the radius gap, lost their envelopes to ‘fill-up’ the first peak at $\sim 1.3R_{\oplus}$.

We also accounted for the fact that luminosities evolve with time as described in [Penz et al. \(2008\)](#) and [Penz & Micela \(2008\)](#). Finally, using this procedure, we retrieved the initial mass thresholds as functions of the orbital distance, for different stellar luminosities, and for M- and G-type stars (in figure 6 and 7 we show the mass threshold functions for a G-type and M-type star respectively for given initial X-ray luminosities). These are the mass limits required for an exoplanet with a certain mass and radius to survive its host stars XUV irradiation throughout its lifetime. During our exoplanet simulations around their host stars we occasionally interpolated between the calculated values of the minimum mass in order to obtain a best-fit curve for each given luminosity.

3.3. Third Path

If an exoplanet makes it to the third stage, it will lose its hydrogen atmosphere. In order to model this, we subtracted the atmospheric mass (given in Equation 2b) from the total planetary mass (M_P). Once the masses had been reduced we then calculated their corresponding radii. Since these planets would lack hydrogen atmospheres, their minimum possible densities are consistent with 100% H_2O ice planets ([Zeng & Sasselov 2013](#); [Zeng et al. 2016](#)), whilst their maximum possible densities are given by the remnant cores of evaporated Neptunian or Jovian planets ([Mocquet et al. 2014](#)). The mean density of our evolved planets was set to an Earth-like silicate planet with a core comprising 30% of the total mass ([Zeng et al. 2016](#)). We distributed the occurrence of each of these compositions according to a laplacian distribution which is shown in Figure 8.

Gas giant or Neptunian remnant core ([Mocquet et al. 2014](#)):

$$\frac{R_{Remnant\ Core}}{R_{\oplus}} = 0.469 \times \left(\frac{M_P}{M_{\oplus}} \right)^{1/3} \quad (4a)$$

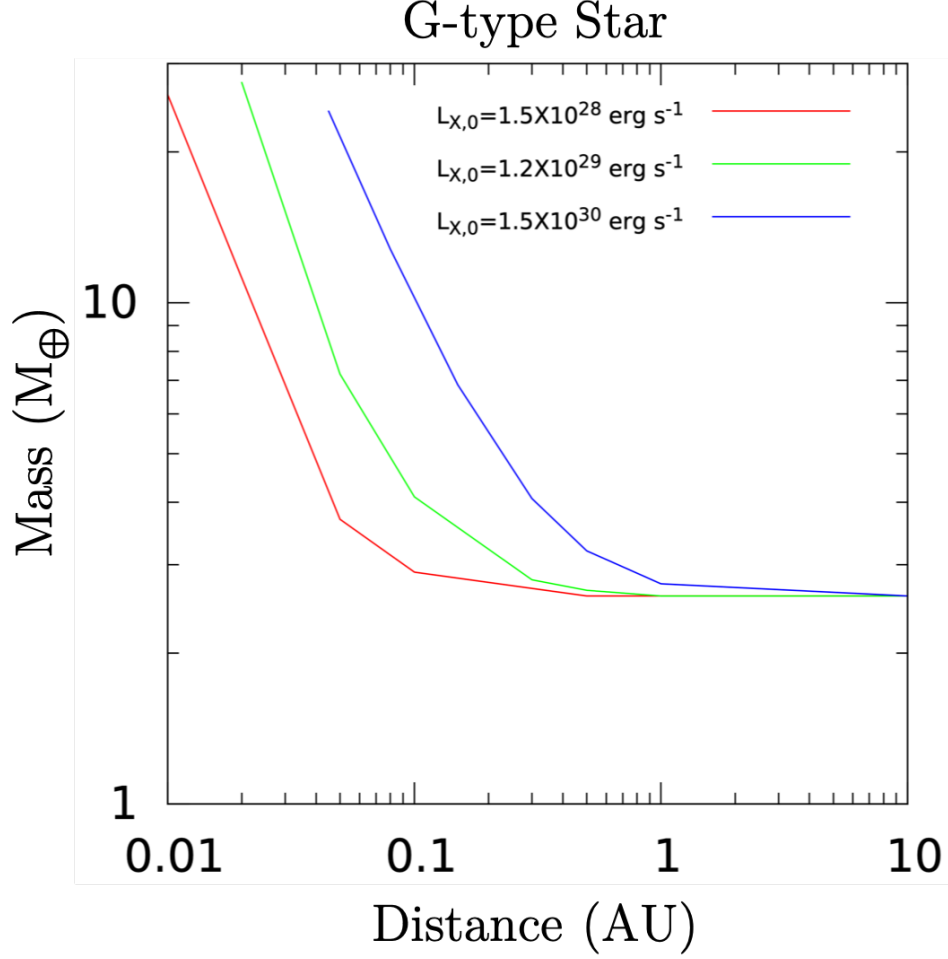


Figure 6. The mass threshold functions calculated using the model from [Locci et al. \(2019\)](#) for G-type stars for different initial X-ray luminosities ([Penz et al. 2008](#)). The UV luminosities scale with the X-ray ones according to the models by [Sanz-Forcada et al. \(2011\)](#).

Terran planet with no atmosphere ([Zeng & Sasselov 2013; Zeng et al. 2016](#)):

$$\frac{R_{Rock}}{R_{\oplus}} = 1.007 \times \left(\frac{M_P}{M_{\oplus}} \right)^{1/3.7} \quad (4b)$$

100% H₂O planet radius ([Zeng & Sasselov 2013; Zeng et al. 2016](#)):

$$\frac{R_{H_2O}}{R_{\oplus}} = 1.410 \times \left(\frac{M_P}{M_{\oplus}} \right)^{1/3.905} \quad (4c)$$

However, if the original (pre-evolution) planetary density was already higher than an Earth-like silicate planet, we also sampled its new radius with a laplace distribution but between the limits set by its pre-evolution radius and the radius of a remnant gas giant/Neptunian core. The mean of the distribution was also set at its pre-evolution radius (see Table 3 for more details). Nevertheless, the majority of newly-formed planets are expected to have densities lower than purely silicate bodies due their primordial envelopes. Consequently, the contribution from these rare exoplanets is expected to be negligible.

Comparing Figure 8 with 3 shows the expected XUV-irradiation-induced evolution in the mass-radius curves of exoplanets. Whilst the original mass and radius plot is centred around the ice or rocky planet with H₂ envelop line, the second plot shows signs of two separate compositions. These being the original low-mass low-density planets, and

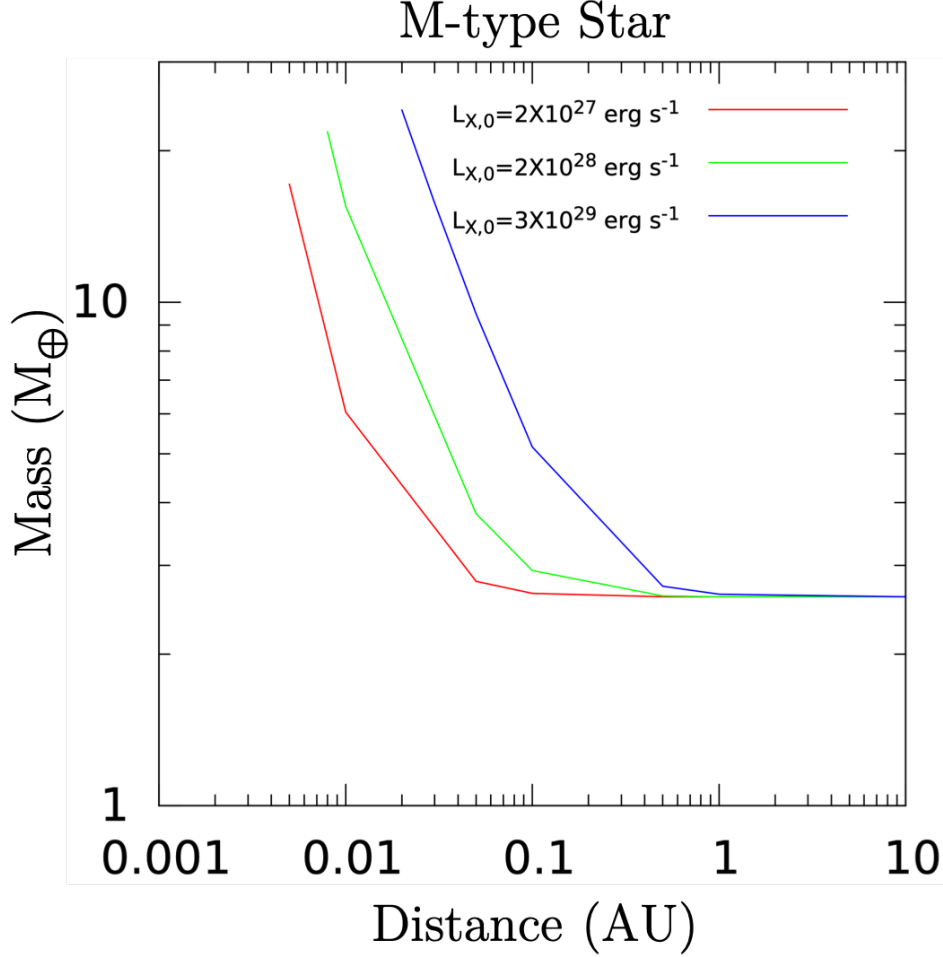


Figure 7. The mass threshold functions calculated using the model from [Locci et al. \(2019\)](#) for M-type stars for different initial X-ray luminosities ([Penz & Micela 2008](#)). The UV luminosities scale with the X-ray ones according to the models by [Sanz-Forcada et al. \(2011\)](#).

rocky worlds. A small gap can also be distinguished between the ice/terran planet with a H_2 envelop line and the Earth-like composition line. Figure 8 follows a similar trend to the mass and radius plot of real exoplanets as shown in Figure 2 of [Zeng et al. \(2018\)](#).

4. RESULTS

After evolving 10^6 exoplanets we are able to replicate the observed bimodal distribution in exoplanet radii with one peak at $\sim 1.3R_\oplus$, the other at $\sim 2.4R_\oplus$, and the minimum at $\sim 1.75R_\oplus$ (see Figure 9). Our results matched well with the observations by ([Fulton et al. 2017](#)) whilst also being consistent with the presence of the sub-Jovian desert (e.g. [Owen & Lai 2018](#)) (see Figures 1 and 12). Furthermore, our final radius distribution is within the error bars given by the data points in Table 3 and Figure 7 of [Fulton et al. \(2017\)](#). Our model predicts that initially most exoplanets were centred around a peak of $\sim 2.4R_\oplus$ that decayed in a laplacian manner as shown in Figure 9. In order to achieve the bimodal behaviour we found that it was mandatory for there to be a paucity of exoplanets $\gtrsim 8M_\oplus$ (see figure 10). For best results we found that this region should be preceded by a flat distribution between $3 - 8M_\oplus$ and another paucity for planets $\lesssim 3M_\oplus$. Because our best-fit initial mass distribution has a lack of planets with $\lesssim 3M_\oplus$, we predict that within the confines of our observations, bodies situated in section α of Equation 2b should be absent or in the very least relatively scarce. With respect to the initial hydrogen envelop masses in Equation 2b, we find best-fit critical masses of $\Upsilon_\alpha = 3M_\oplus$, $\Upsilon_\beta = 10M_\oplus$ with the probabilistic functions Γ_β and Γ_γ detailed in Table 3.

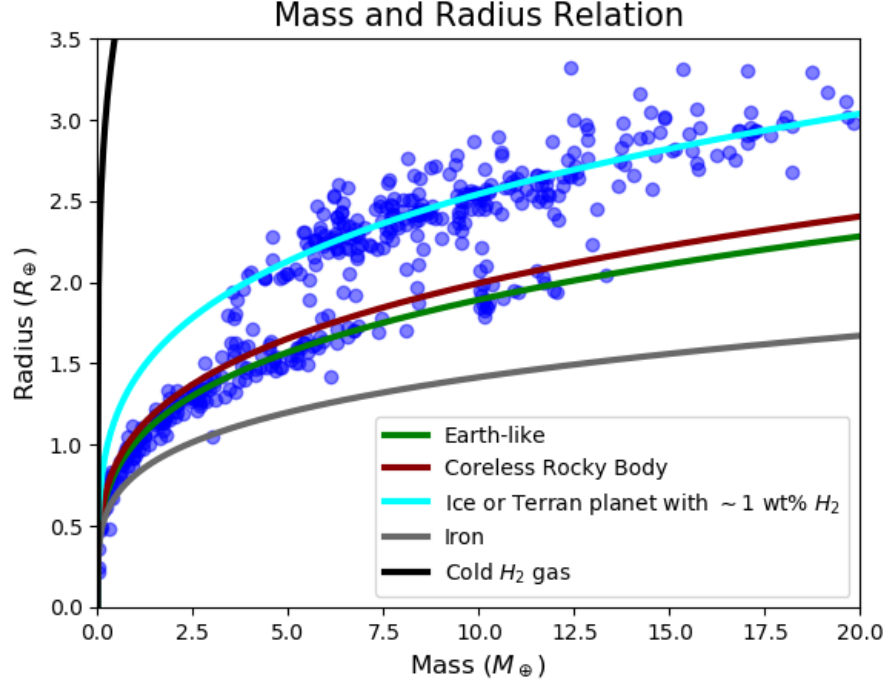


Figure 8. The mass and radius distribution of 500 of our synthetic exoplanets after undergoing photoevaporation. All mass and radius curves come from Zeng & Sasselov (2013) and Zeng et al. (2016) except for the cold H_2 curve which originated from the equations of state by Becker et al. (2014) that were then adapted by Zeng et al. (2018). The scale parameter of the laplacian function of the radii was set to 0.05 (i.e. a standard deviation of $\sqrt{2}/20$.)

Regarding the final mass distribution (see Figure 10), for masses greater than $\sim 11.5M_{\oplus}$ the difference between the initial and final distribution is very small. This is because with bigger masses it becomes exceedingly harder to remove the primordial hydrogen envelopes of exoplanets due to their stronger gravitational strengths. From $10 - 11.5M_{\oplus}$ we predict a small increase in the abundance which is caused by the remnant cores of Neptunian or Jovian planets (more details on this can be found in section 5). From $3 - 10M_{\oplus}$ there is a strong decrease in the mass abundance which is caused by planets with cores $\lesssim 3M_{\oplus}$ losing the entirety of their envelopes. After the XUV-induced evolution of these planets, the increase in the number of bodies with $\lesssim 3M_{\oplus}$ corresponds with the radius peak at $\sim 1.3R_{\oplus}$ (Zeng & Sasselov 2013; Zeng et al. 2016). In spite of the increase in rocky worlds with masses at $\sim 10M_{\oplus}$ matching the small peak at $1.95R_{\oplus}$ (despite the uncertainties being large, this is consistent with the $1.77 - 1.97R_{\oplus}$ abundance measured by Fulton et al. (2017)), the overall number of planets with radii of $\sim 1.95R_{\oplus}$ has decreased. This is because despite the increase in rocky cores at $\sim 1.95R_{\oplus}$, planets with hydrogen envelopes previously located in this region decreased more numerous. Concerning with the radius peak at $\sim 2.4R_{\oplus}$, this is compatible with rocky planets sustaining hydrogen envelopes where the combined total mass is $\sim 8M_{\oplus}$. According to Zeng & Sasselov (2013); Zeng et al. (2016) An airless rocky planet with the same mass would instead be located at $\sim 1.9R_{\oplus}$ which lies in the region of the remnant Neptunian and Jovian cores explained above. With respect to the density evolution our simulation shows that on average the planet densities increased sharply which can be seen in Figure 11. Numerically, our results can be summarised as follows with the best-fit input distributions shown in Table 3:

1. $\sim 11\%$ of known exoplanets are currently in the processes of losing their atmospheres (first path).
2. $\sim 46\%$ of exoplanets have the right orbital and physical properties required in order for their primordial envelopes to outlive their host star's lifetime (second path).
3. $\sim 43\%$ of exoplanets completely lost their primordial hydrogen envelopes (third path).

5. DISCUSSIONS

Table 3. Adopted Input Distributions.

Exoplanet Property	Functional Form	Parameters
Orbital Distance	Lognormal	<ul style="list-style-type: none"> • Max = 100 days • Min = $R_{\text{Roche}} \sim 2R_*$ • $\mu \approx -1$ • $\sigma \approx 0.3$
Initial Mass	$= \begin{cases} \text{Uniform} & 3M_{\oplus} \leq M_P < 8M_{\oplus} \\ \text{Pareto} & 8M_{\oplus} \leq M_P \leq 25M_{\oplus} \end{cases}$	<u>Pareto</u> <ul style="list-style-type: none"> • Mo = $8.0M_{\oplus}$ • a = 1.6
Initial Compositions	Laplace	<ul style="list-style-type: none"> • Max = Eq. 1c • Min = Eq. 1a • μ = Eq. 1b • b = $\sqrt{2}\sigma = 0.1R_{\oplus}$
Ages	Trunc. Normal	<ul style="list-style-type: none"> • Max = 13.51 Gyr • Min = 0.25 Gyr • $\mu \approx 2.9$ Gyr • $\sigma = 4.3$ Gyr
Γ_{β} (Eq. 2b)	Uniform	<ul style="list-style-type: none"> • Max = M_P • Min = 0
Γ_{γ} (Eq. 2b)	Pareto	<ul style="list-style-type: none"> • Max = M_P • Min = 0 • Mo = $10M_{\oplus}$ • a = 1
Final Compositions	Laplace	<u>$R_{\text{Initial}} > \text{Eq. 4b}$</u> <ul style="list-style-type: none"> • Max = Eq. 4c • Min = Eq. 4a • μ = Eq. 4b • b = $\sqrt{2}\sigma = 0.05R_{\oplus}$ <u>$R_{\text{Initial}} < \text{Eq. 4b}$</u> <ul style="list-style-type: none"> • Max = R_{Initial} • Min = Eq. 4a • $\mu = R_{\text{Initial}}$ • b = $\sqrt{2}\sigma = 0.05R_{\oplus}$

NOTE—Mo = Mode, μ = arithmetic mean, σ = standard deviation, a = shape, b = scale, Max and Min are the maximum and minimum limits respectively.

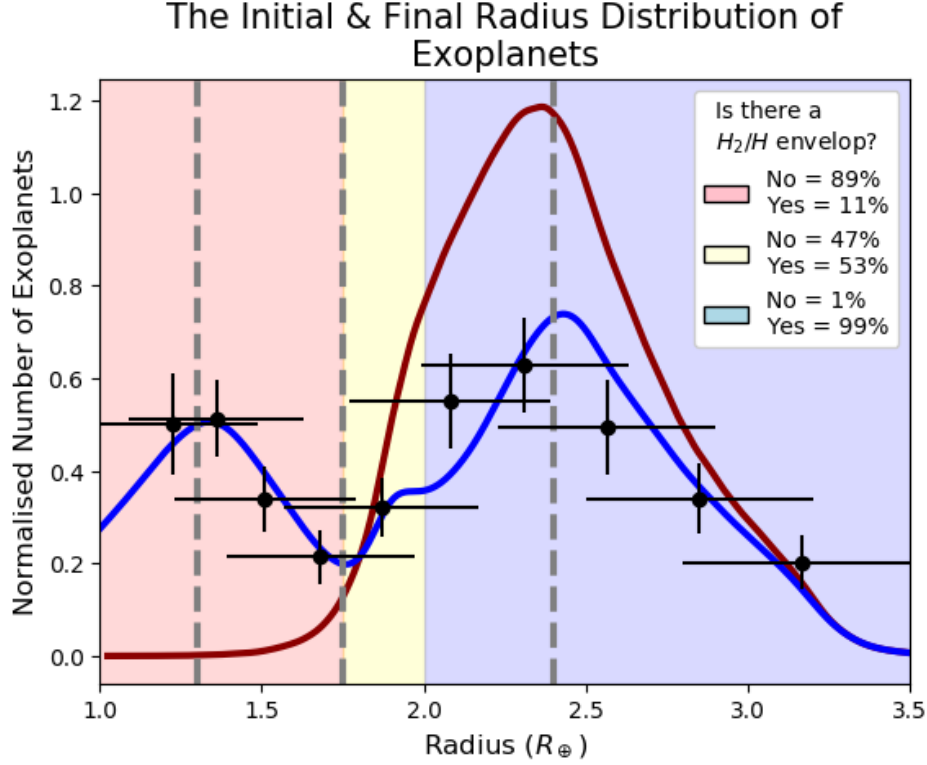


Figure 9. The final (blue line) and initial (red line) distributions of exoplanet radii for periods ≤ 100 days obtained by our model. The grey lines show the two peaks and the minimum discovered by [Fulton et al. \(2017\)](#). The data points with the uncertainties correspond to the values given in Table 3 and Figure 7 of [Fulton et al. \(2017\)](#). The light-red, light-yellow and light-blue regions correspond only to the final radius distribution’s rocky first peak, the remnant core (mega-Earth)-rich region, and the hydrogen-rich worlds of the second peak respectively. For each region we report the planet population composition.

Overall our results are similar to those of [Owen & Wu \(2013, 2017\)](#) where the observed radial distribution was caused due to stellar XUV irradiation triggering atmospheric erosion. However, the differences are due to us adopting the core compositional models of [Zeng & Sasselov \(2013\)](#); [Zeng et al. \(2016\)](#) and [Mocquet et al. \(2014\)](#) which use considerably different equations of state. Our code also predicts a small but non-negligible contribution from large remnant cores (i.e. mega-Earths) formed from the removal of large hydrogen atmospheres from Neptunian-planets. We argue that most of these remnant cores are of mass $\sim 10M_{\oplus}$ which for decompressed relaxed cores (which occurs after \sim few Gyrs) corresponds to radii within the range $1.77 - 1.97R_{\oplus}$. This result is compatible with [Swain et al. \(2019\)](#) that identified a “transition region” rich in terrestrial and hydrogen-bearing planets between $1.5R_{\oplus} - 2.0R_{\oplus}$. As explained in section 2.3 some remnant cores may be much larger which is corroborated by observational evidence and a strong theoretical foundation. These larger mega-Earths have radii that are located within the $\sim 2.4R_{\oplus}$ peak implying that this larger peak is dominated by planets with large hydrogen envelopes ($\sim 99\%$) with a few massive mega-Earths ($\sim 1\%$).

Regarding the composition of each peak, to a very tight standard deviation (see Figures 3 and 8 for a visual representation, and Table 3 for the numerical values) we find that most planets in the first peak ($\sim 1.3R_{\oplus}$) are rocky and without a primordial atmosphere which agrees with the results from [Owen & Wu \(2013, 2017\)](#), [Jin & Mordasini \(2018\)](#) and [Swain et al. \(2019\)](#). Conversely, we find that most planets in the second peak ($\sim 2.4R_{\oplus}$) have large primordial envelopes. Notwithstanding, there are exceptions such as Fe planets with small hydrogen atmospheres that could lay in the first peak or denuded H_2O ice planets that have very low densities and therefore may lay in the second peak ([Zeng et al. 2018](#)) but these are very scarce. We believe that our predicted initial distribution of exoplanet radii (figure 9) makes conceptual sense as most planets are born with large hydrogen depositories which results in their large puffy radii. Of these planets, very few have unusually small radii (i.e. small atmospheres) or unusually large radii (i.e. large atmospheres) which results in the initial distribution looking laplacian in nature.

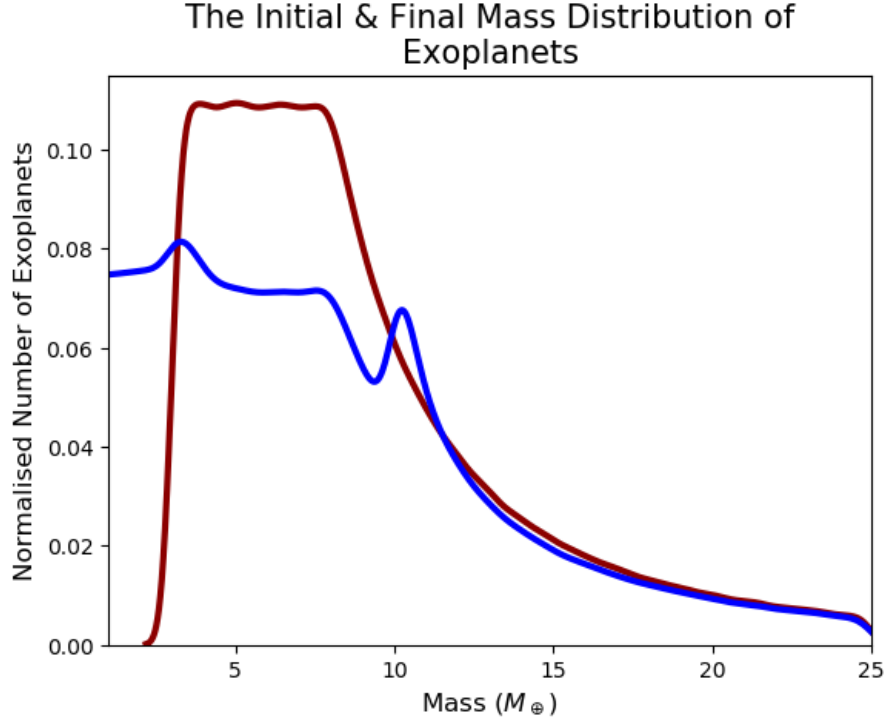


Figure 10. The predicted final (blue) and initial (red) mass distributions of exoplanets whose current radii are distributed according to Fig 9. All planets have periods ≤ 100 days.

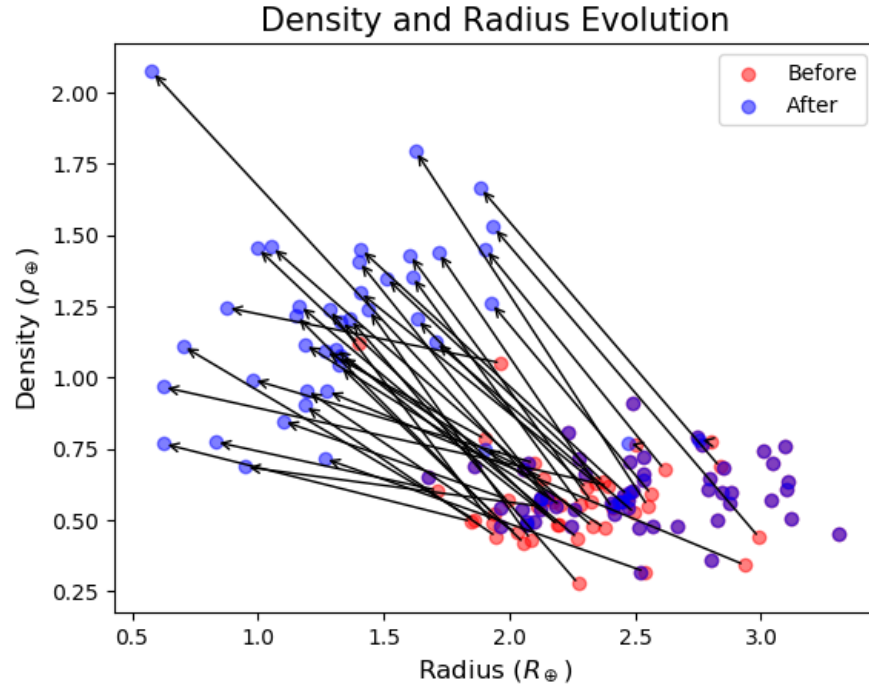


Figure 11. A plot showing the density and radius evolution of 100 randomly chosen exoplanets.

One major difference between our paper and [Owen & Wu \(2017\)](#) is our predicted initial mass distributions of exoplanets. In their paper, their mass function follows a Rayleigh distribution with a mode at $3M_{\oplus}$. When we adopted

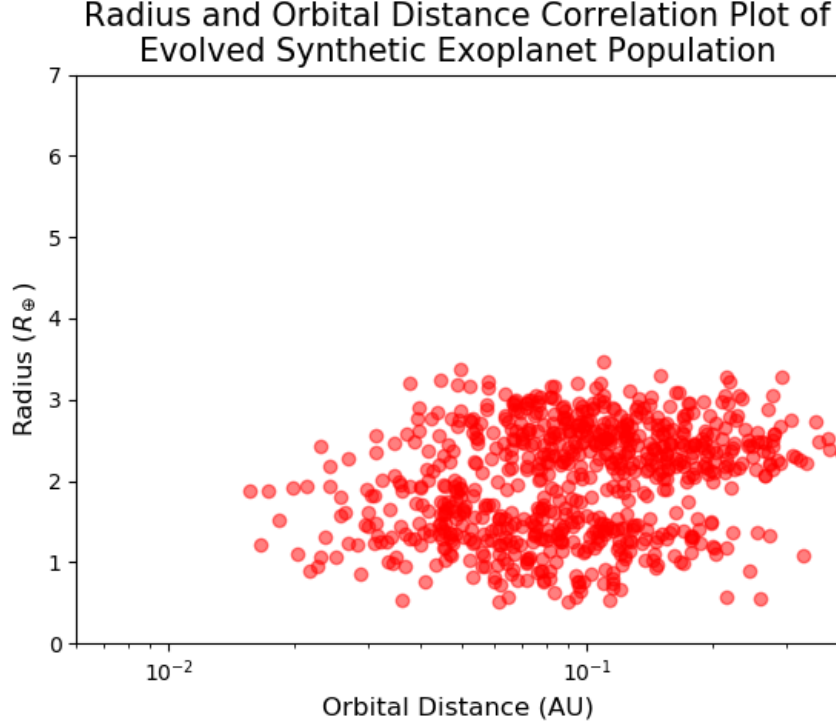


Figure 12. A plot of the radius and orbital distance of 787 (for comparison with Figure 1) randomly chosen exoplanets.

the same distribution we were unable to generate the bimodal behaviour with the right amplitudes at each peak (see Figure 13). This disparity is explained by the intrinsic nature of Rayleigh distributions which generally produce a large number of values relatively close to zero. According to our simulations in order to achieve a distribution emulating the one by [Fulton et al. \(2017\)](#) it is necessary for there to be a deficiency in planets with small masses so a Rayleigh function is not appropriate. In addition, our best-fit initial mass distribution requires a lack of exoplanets with masses $\gtrsim 8M_{\oplus}$. According to our simulations, this lack of Neptunian-mass bodies is independent of stellar XUV irradiation. This drop in the occurrence rate of larger mass exoplanets is consistent with observations (e.g. [Howard et al. 2010](#); [Marcy et al. 2014](#); [Malhotra 2015](#)). In addition, a paucity in exoplanet masses beyond $\sim 10M_{\oplus}$ has been predicted by several planetary formation models (e.g. [Ida & Lin 2004, 2005, 2008](#); [Mordasini et al. 2009](#)) as at this critical size efficient accretion of materials results in few bodies having intermediate masses between $10 - 100M_{\oplus}$. Concerning with the flat distribution between $0 - 8M_{\oplus}$, this was not mandatory for a bimodal distribution in the radii, but it gave us a better fit than our best-fit truncated gaussian function (see Figure 13). There are several processes that could give rise to this result. One potential explanation is that even though small cores are more common than larger ones (e.g. [Schlichting et al. 2013](#); [Simon et al. 2016](#)), they are also harder to detect. Planets with smaller masses not only accrete less primordial gas (e.g. [Stevenson 1999](#); [Ikoma & Hori 2012](#); [Chachan & Stevenson 2018](#)), but they are also more susceptible to atmospheric destruction. In addition, they are also more likely to be ejected from their planetary systems because of gravitational perturbations. This is particularly true if giant planets are present in the system, with simulations predicting that on average each star ejects ~ 7.9 planets of which ~ 2.5 are terrestrial in size ([Barclay et al. 2017](#)). Although the exact demographics of rogue planets are a subject of dispute, it is generally accepted that there are at least billions in the Milky Way galaxy (e.g. [Levison et al. 1998](#); [Chambers & Wetherill 1998](#); [Debes & Sigurdsson 2007](#)). Furthermore, at very close distances to the host star (i.e. $\lesssim 1$ AU) there is a scarcity of solids which limits the growth of planetesimals (e.g. [Lodders 2003](#); [Mordasini et al. 2009](#)). Consequently, most seed embryos can only form beyond the ice line (e.g. [Podolak & Zucker 2004](#); [Martin & Livio 2012](#); [D’Angelo & Podolak 2015](#)). However, fast type 1 migration means that the depletion in planets with $3M_{\oplus} \lesssim M_p \lesssim 10M_{\oplus}$ disappears because bodies initially orbiting farther out move inwards ([Mordasini et al. 2009](#)). This implies that super-Earths and sub-Neptunes with masses $\lesssim 3M_{\oplus}$ would be preferentially depleted in comparison with heavier mass bodies. Since this reduction is mostly prevalent at shorter distances and we have an observational bias towards close-orbiting exoplanets;

this decrease should be more pronounced. It is therefore possible that for smaller exoplanets; detection biases, more efficient ejections, and their predicted lack of fast type 1 migration could cancel out with their intrinsically larger populations which results in a perceived initial flat mass function. Despite our initial mass function differing from Owen & Wu (2017), we predict an almost identical distribution to Ginzburg et al. (2018) even though their mass-loss mechanism is considerably different to ours. Their model argues for a broken power-law which is flat from $0 - 5M_{\oplus}$ and then approaches zero for cores $> 5M_{\oplus}$. We predict a slightly extended flat region but the overall shape is in strong agreement.

With regards to our final mass function, it grows rapidly for smaller masses which is compatible with the observations from Howard et al. (2010). The small peak at $\sim 3M_{\oplus}$ is due to a collection of planets with and without hydrogen envelopes located in that region. Furthermore, the small maximum at $\sim 8M_{\oplus}$ is consistent with the observed mass peak of the *Kepler* planets as shown by Marcy et al. (2014) and Malhotra (2015). However, even though the observed mass distribution is in agreement with our model, we are aware that the actual mass distribution of *Kepler* planets has not been reliably determined due to the difficulty of obtaining the masses of small exoplanets.

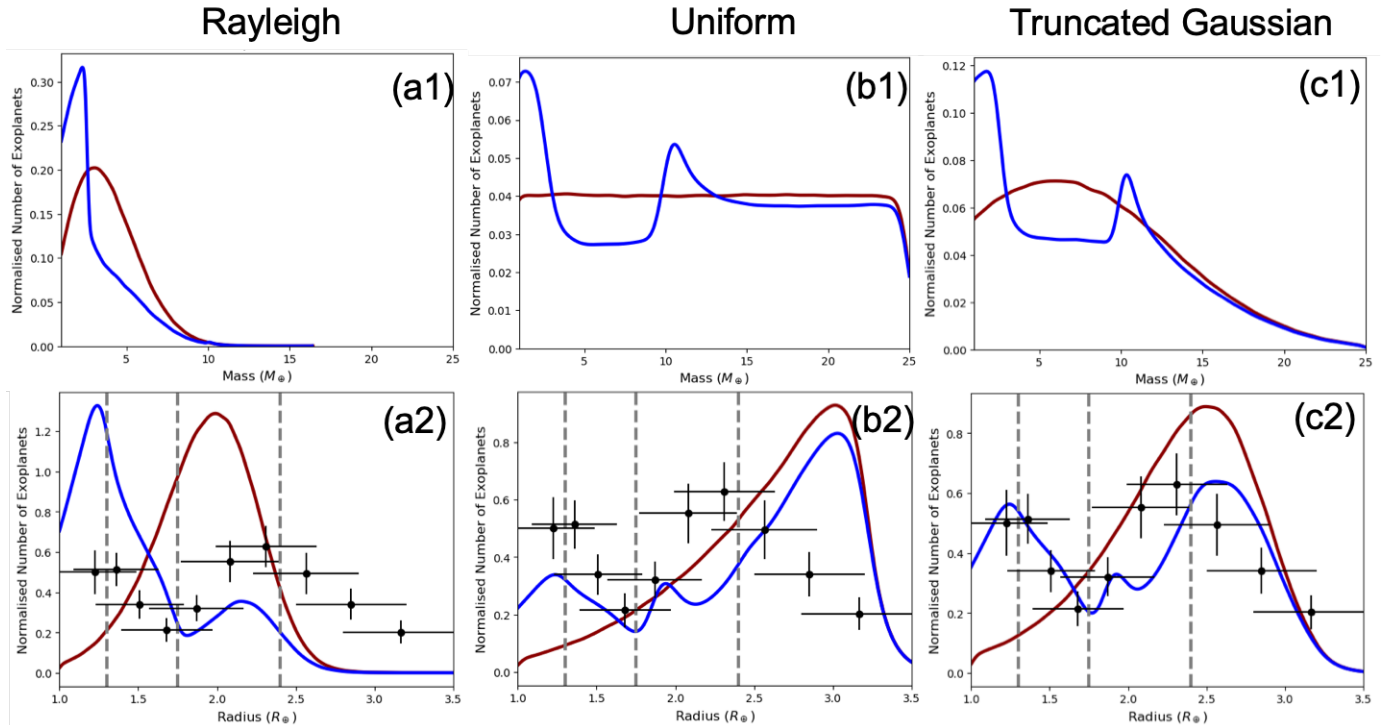


Figure 13. A plot showing the initial (red) and final (blue) mass (a1, b1, c1) and radius (a2, b2, c2) functions. The truncated gaussian function for the mass distribution (c1) has a mean of $6M_{\oplus}$, a standard deviation of $7M_{\oplus}$, and a minimum and maximum limit of 0.1 and $25M_{\oplus}$ respectively.

In Figure 13 we show how the final radius and mass distribution would change depending on our initial mass function. Our simulations show that the best fit curve is a flat region from $3 - 8M_{\oplus}$ followed by a pareto distribution as shown in figure 10. The truncated gaussian mass function shown in Figure 13 provides a possible alternative to our model especially because the observations by Fulton et al. (2017) have considerable uncertainties. However, we found that the major problem with a truncated gaussian function was the shape of the tail in relation to the position of the second radius peak. We were unable to get a fit where the location of the second peak lay at $\sim 2.4R_{\oplus}$ whilst at the same time matching the shape of the tail of the distribution. We also tried to fit a truncated laplace distribution (not shown in the manuscript) to the initial masses but our results were similar (albeit slightly worse) to the truncated gaussian distribution. Finally, we show that without a deficiency in the occurrence rate at larger masses (i.e. $\gtrsim 8M_{\oplus}$), the bimodal distribution is strongly distorted and does not match the observations by Fulton et al. (2017).

5.1. Limitations of our Model

When dealing with studies that are deeply theoretical such as this one it is crucial to consider the initial parameters and assumptions made since they can greatly affect the results. Due to the bimodal distribution of exoplanet radii being a multivariate phenomenon with a deeply stochastic nature it is not possible to test every parameter combination so assumptions were inevitable. One such assumption was that exoplanet orbital distances did not evolve and therefore remained constant. This is certainly false since many different effects can lead to large scale planetary migration such as (and not limited to):

1. Gravitational scattering due to overdensities caused by other planets in the vicinity (e.g. [Hansen & Zink 2015](#)).
2. In a binary system or when there are two planets with different inclinations, the Kozai mechanism can cause the planet in question to exchange eccentricity and inclination resulting in tidal friction and a subsequent shrinking of the orbital distance (e.g. [Kozai 1962](#); [Nagasawa et al. 2008](#); [Naoz et al. 2011](#)).
3. Tidal migration. For example, a planet orbiting very close to its host star may induce a bulge which could lead to a loss in angular momentum if the star rotates faster than the planet’s orbital period (e.g. [Jackson et al. 2008](#); [Penev & Sasselov 2010, 2011](#)).

Points 1 and 2 normally occur rapidly ($\ll 1$ Gyr) whilst 3 occurs on a longer timescale (\sim few Gyr). Other aspects we ignored include, but are not limited to: how for close-orbiting tidally locked super-Earths, the tidal forces, together with the orbital and rotational centrifugal forces, could partially confine a hydrogen-rich atmosphere on the nightside ([Modirrousta-Galian et al. 2020](#)); secondary atmospheres and how they affect the radii of exoplanets; meteorite impacts and how they can influence atmospheres (e.g. [Miller-Ricci et al. 2009](#); [Lupu et al. 2014](#)); star mergers forming disks from which planets can form (e.g. [Tutukov 1991](#); [Martin et al. 2011](#)); and planet-planet collisions (e.g. [Ji et al. 2011](#); [Chrenko et al. 2018](#)). These mechanisms are not only very hard to model, but most probably negligible and/or statistically insignificant.

6. CONCLUSIONS

After exposing 10^6 synthetic exoplanets to their host star’s XUV irradiation we show that the bimodal distribution observed by [Fulton et al. \(2017\)](#) can be reproduced. Our results indicate that for the radius gap to exist it is essential for there to be an initial paucity of exoplanets with masses $\gtrsim 8M_{\oplus}$. Furthermore, our best fit results suggest that there is a flat distribution of exoplanets with masses $3M_{\oplus} - 8M_{\oplus}$ and a paucity for planets with masses $\lesssim 3M_{\oplus}$. In other words, the initial distribution of exoplanet masses, has a great influence on the final radius distribution. With regards to the properties of the radius distribution, we predict that the peak situated at $\sim 1.3R_{\oplus}$ consists mostly of rocky denuded bodies whilst the maximum at $\sim 2.4R_{\oplus}$ marks a region full of hydrogen-rich exoplanets with a few mega-Earths. There are some very rare exceptions such as metallic planets with small hydrogen atmospheres and denuded H_2O ice planets ([Zeng et al. 2018](#)) which could lay in the first and second peak respectively. Finally, we believe that our predictions can be tested in the not too distant future due to rapid technological advances. For instance, the James Webb Space Telescope (JWST), Atmospheric Remote-sensing Infrared Exoplanet Large-survey (ARIEL), Thirty Meter Telescope (TMT), and Extremely Large Telescope (ELT) should become active in the next few years which would allow for far superior exoplanet observations. In the future, statistical methods on large data sets could be used in contrast to analysing individual cases like at the present. For instance, with Tier 1 of ARIEL we could test the exoplanets at each peak on whether or not they have an atmosphere; this would provide strong evidence for or against our results. Furthermore, if we can get more unbiased mass distribution measurements for super-Earths and sub-Neptunes through Earth-based observations, this would be a strong test for the validity of our model.

ACKNOWLEDGEMENTS

We acknowledge the support of the ARIEL ASI-INAF agreement n.2018-22-HH.0. We thank P. Neague and the anonymous referee for their useful comments.

REFERENCES

- | | |
|---|--|
| <p>Aggarwal, H. R., & Oberbeck, V. R. 1974, <i>ApJ</i>, 191, 577,
doi: 10.1086/152998</p> | <p>Barclay, T., Quintana, E. V., Raymond, S. N., & Penny,
M. T. 2017, <i>ApJ</i>, 841, 86, doi: 10.3847/1538-4357/aa705b</p> |
|---|--|

- Becker, A., Lorenzen, W., Fortney, J. J., et al. 2014, *ApJS*, 215, 21, doi: [10.1088/0067-0049/215/2/21](https://doi.org/10.1088/0067-0049/215/2/21)
- Chabrier, G., Saumon, D., Hubbard, W. B., & Lunine, J. I. 1992, *ApJ*, 391, 817, doi: [10.1086/171390](https://doi.org/10.1086/171390)
- Chachan, Y., & Stevenson, D. J. 2018, *ApJ*, 854, 21, doi: [10.3847/1538-4357/aaa459](https://doi.org/10.3847/1538-4357/aaa459)
- Chambers, J. E., & Wetherill, G. W. 1998, *Icarus*, 136, 304, doi: [10.1006/icar.1998.6007](https://doi.org/10.1006/icar.1998.6007)
- Chrenko, O., Brož, M., & Nesvorný, D. 2018, *ApJ*, 868, 145, doi: [10.3847/1538-4357/aaeb93](https://doi.org/10.3847/1538-4357/aaeb93)
- D’Angelo, G., & Podolak, M. 2015, *ApJ*, 806, 203, doi: [10.1088/0004-637X/806/2/203](https://doi.org/10.1088/0004-637X/806/2/203)
- Debes, J. H., & Sigurdsson, S. 2007, *ApJL*, 668, L167, doi: [10.1086/523103](https://doi.org/10.1086/523103)
- Ehrenreich, D., & Désert, J.-M. 2011, *A&A*, 529, A136, doi: [10.1051/0004-6361/201016356](https://doi.org/10.1051/0004-6361/201016356)
- Erkaev, N. V., Kulikov, Y. N., Lammer, H., et al. 2007, *A&A*, 472, 329, doi: [10.1051/0004-6361:20066929](https://doi.org/10.1051/0004-6361:20066929)
- Espinoza, N., Brahm, R., Jordán, A., et al. 2016, *ApJ*, 830, 43, doi: [10.3847/0004-637X/830/1/43](https://doi.org/10.3847/0004-637X/830/1/43)
- Fulton, B. J., Petigura, E. A., Howard, A. W., et al. 2017, *AJ*, 154, 109, doi: [10.3847/1538-3881/aa80eb](https://doi.org/10.3847/1538-3881/aa80eb)
- Ginzburg, S., Schlichting, H. E., & Sari, R. 2016, *ApJ*, 825, 29, doi: [10.3847/0004-637X/825/1/29](https://doi.org/10.3847/0004-637X/825/1/29)
- . 2018, *MNRAS*, 476, 759, doi: [10.1093/mnras/sty290](https://doi.org/10.1093/mnras/sty290)
- Gudkova, T. V., & Zharkov, V. N. 1999, *Planet. Space Sci.*, 47, 1201, doi: [10.1016/S0032-0633\(99\)00044-6](https://doi.org/10.1016/S0032-0633(99)00044-6)
- Guillot, T. 1999, *Planet. Space Sci.*, 47, 1183, doi: [10.1016/S0032-0633\(99\)00043-4](https://doi.org/10.1016/S0032-0633(99)00043-4)
- Guillot, T., Gautier, D., & Hubbard, W. B. 1997, *Icarus*, 130, 534, doi: [10.1006/icar.1997.5812](https://doi.org/10.1006/icar.1997.5812)
- Gupta, A., & Schlichting, H. E. 2018, arXiv e-prints, <https://arxiv.org/abs/1811.03202>
- Hansen, B. M. S., & Zink, J. 2015, *MNRAS*, 450, 4505, doi: [10.1093/mnras/stv916](https://doi.org/10.1093/mnras/stv916)
- Hayashi, C., Nakazawa, K., & Nakagawa, Y. 1985, in *Protostars and Planets II*, ed. D. C. Black & M. S. Matthews, 1100–1153
- Howard, A. W., Marcy, G. W., Johnson, J. A., et al. 2010, *Science*, 330, 653, doi: [10.1126/science.1194854](https://doi.org/10.1126/science.1194854)
- Hubbard, W. B., & Marley, M. S. 1989, *Icarus*, 78, 102, doi: [10.1016/0019-1035\(89\)90072-9](https://doi.org/10.1016/0019-1035(89)90072-9)
- Ida, S., & Lin, D. N. C. 2004, *ApJ*, 604, 388, doi: [10.1086/381724](https://doi.org/10.1086/381724)
- . 2005, *ApJ*, 626, 1045, doi: [10.1086/429953](https://doi.org/10.1086/429953)
- . 2008, *ApJ*, 685, 584, doi: [10.1086/590401](https://doi.org/10.1086/590401)
- Ikoma, M., & Hori, Y. 2012, *ApJ*, 753, 66, doi: [10.1088/0004-637X/753/1/66](https://doi.org/10.1088/0004-637X/753/1/66)
- Jackson, B., Greenberg, R., & Barnes, R. 2008, *ApJ*, 681, 1631, doi: [10.1086/587641](https://doi.org/10.1086/587641)
- Ji, J., Jin, S., & Tinney, C. G. 2011, *ApJL*, 727, L5, doi: [10.1088/0004-637X/727/1/L5](https://doi.org/10.1088/0004-637X/727/1/L5)
- Jin, S., & Mordasini, C. 2018, *ApJ*, 853, 163, doi: [10.3847/1538-4357/aa9fle](https://doi.org/10.3847/1538-4357/aa9fle)
- Jin, S., Mordasini, C., Parmentier, V., et al. 2014, *ApJ*, 795, 65, doi: [10.1088/0004-637X/795/1/65](https://doi.org/10.1088/0004-637X/795/1/65)
- Kozai, Y. 1962, *AJ*, 67, 591, doi: [10.1086/108790](https://doi.org/10.1086/108790)
- Kubyschkina, D., Fossati, L., Erkaev, N. V., et al. 2018a, *A&A*, 619, A151, doi: [10.1051/0004-6361/201833737](https://doi.org/10.1051/0004-6361/201833737)
- . 2018b, *ApJL*, 866, L18, doi: [10.3847/2041-8213/aae586](https://doi.org/10.3847/2041-8213/aae586)
- Lammer, H., Erkaev, N. V., Odert, P., et al. 2013, *MNRAS*, 430, 1247, doi: [10.1093/mnras/sts705](https://doi.org/10.1093/mnras/sts705)
- Lecavelier Des Etangs, A. 2007, *A&A*, 461, 1185, doi: [10.1051/0004-6361:20065014](https://doi.org/10.1051/0004-6361:20065014)
- Levison, H. F., Lissauer, J. J., & Duncan, M. J. 1998, *AJ*, 116, 1998, doi: [10.1086/300557](https://doi.org/10.1086/300557)
- Locci, D., Cecchi-Pestellini, C., & Micela, G. 2019, *A&A*, 624, A101, doi: [10.1051/0004-6361/201834491](https://doi.org/10.1051/0004-6361/201834491)
- Lodders, K. 2003, *ApJ*, 591, 1220, doi: [10.1086/375492](https://doi.org/10.1086/375492)
- Lupu, R. E., Zahnle, K., Marley, M. S., et al. 2014, *ApJ*, 784, 27, doi: [10.1088/0004-637X/784/1/27](https://doi.org/10.1088/0004-637X/784/1/27)
- Malhotra, R. 2015, *ApJ*, 808, 71, doi: [10.1088/0004-637X/808/1/71](https://doi.org/10.1088/0004-637X/808/1/71)
- Marcy, G. W., Isaacson, H., Howard, A. W., et al. 2014, *ApJS*, 210, 20, doi: [10.1088/0067-0049/210/2/20](https://doi.org/10.1088/0067-0049/210/2/20)
- Martin, E. L., Spruit, H. C., & Tata, R. 2011, *A&A*, 535, A50, doi: [10.1051/0004-6361/201116907](https://doi.org/10.1051/0004-6361/201116907)
- Martin, R. G., & Livio, M. 2012, *MNRAS*, 425, L6, doi: [10.1111/j.1745-3933.2012.01290.x](https://doi.org/10.1111/j.1745-3933.2012.01290.x)
- Miller-Ricci, E., Meyer, M. R., Seager, S., & Elkins-Tanton, L. 2009, *ApJ*, 704, 770, doi: [10.1088/0004-637X/704/1/770](https://doi.org/10.1088/0004-637X/704/1/770)
- Mizuno, H. 1980, *Progress of Theoretical Physics*, 64, 544, doi: [10.1143/PTP.64.544](https://doi.org/10.1143/PTP.64.544)
- Mocquet, A., Grasset, O., & Sotin, C. 2014, *Philosophical Transactions of the Royal Society of London Series A*, 372, 20130164, doi: [10.1098/rsta.2013.0164](https://doi.org/10.1098/rsta.2013.0164)
- Modirrousta-Galian, D., Locci, D., Tinetti, G., & Micela, G. 2020, *The Astrophysical Journal*, 888, 87, doi: [10.3847/1538-4357/ab616b](https://doi.org/10.3847/1538-4357/ab616b)
- Moll, R., Garaud, P., Mankovich, C., & Fortney, J. J. 2017, *ApJ*, 849, 24, doi: [10.3847/1538-4357/aa8d74](https://doi.org/10.3847/1538-4357/aa8d74)
- Mordasini, C., Alibert, Y., & Benz, W. 2009, *A&A*, 501, 1139, doi: [10.1051/0004-6361/200810301](https://doi.org/10.1051/0004-6361/200810301)
- Nagasawa, M., Ida, S., & Bessho, T. 2008, *ApJ*, 678, 498, doi: [10.1086/529369](https://doi.org/10.1086/529369)
- Naoz, S., Farr, W. M., Lithwick, Y., Rasio, F. A., & Teyssandier, J. 2011, *Nature*, 473, 187, doi: [10.1038/nature10076](https://doi.org/10.1038/nature10076)

- Owen, J. E., & Lai, D. 2018, *MNRAS*, 479, 5012, doi: [10.1093/mnras/sty1760](https://doi.org/10.1093/mnras/sty1760)
- Owen, J. E., & Wu, Y. 2013, *ApJ*, 775, 105, doi: [10.1088/0004-637X/775/2/105](https://doi.org/10.1088/0004-637X/775/2/105)
- . 2017, *ApJ*, 847, 29, doi: [10.3847/1538-4357/aa890a](https://doi.org/10.3847/1538-4357/aa890a)
- Penev, K., & Sasselov, D. 2011, *ApJ*, 731, 67, doi: [10.1088/0004-637X/731/1/67](https://doi.org/10.1088/0004-637X/731/1/67)
- Penev, K., & Sasselov, D. D. 2010, in *Bulletin of the American Astronomical Society*, Vol. 42, American Astronomical Society Meeting Abstracts #215, 328
- Penz, T., & Micela, G. 2008, *A&A*, 479, 579, doi: [10.1051/0004-6361:20078873](https://doi.org/10.1051/0004-6361:20078873)
- Penz, T., Micela, G., & Lammer, H. 2008, *A&A*, 477, 309, doi: [10.1051/0004-6361:20078364](https://doi.org/10.1051/0004-6361:20078364)
- Podolak, M., & Zucker, S. 2004, *Meteoritics and Planetary Science*, 39, 1859, doi: [10.1111/j.1945-5100.2004.tb00081.x](https://doi.org/10.1111/j.1945-5100.2004.tb00081.x)
- Sanz-Forcada, J., Micela, G., Ribas, I., et al. 2011, *A&A*, 532, A6, doi: [10.1051/0004-6361/201116594](https://doi.org/10.1051/0004-6361/201116594)
- Schlichting, H. E., Fuentes, C. I., & Trilling, D. E. 2013, *AJ*, 146, 36, doi: [10.1088/0004-6256/146/2/36](https://doi.org/10.1088/0004-6256/146/2/36)
- Shibata, S., & Ikoma, M. 2019, *MNRAS*, 487, 4510, doi: [10.1093/mnras/stz1629](https://doi.org/10.1093/mnras/stz1629)
- Shiraishi, M., & Ida, S. 2008, *ApJ*, 684, 1416, doi: [10.1086/590226](https://doi.org/10.1086/590226)
- Siess, L., Dufour, E., & Forestini, M. 2000, *A&A*, 358, 593
- Simon, J. B., Armitage, P. J., Li, R., & Youdin, A. N. 2016, *ApJ*, 822, 55, doi: [10.3847/0004-637X/822/1/55](https://doi.org/10.3847/0004-637X/822/1/55)
- Sinukoff, E., Howard, A. W., Petigura, E. A., et al. 2017, *AJ*, 153, 271, doi: [10.3847/1538-3881/aa725f](https://doi.org/10.3847/1538-3881/aa725f)
- Stevenson, D. J. 1982, *Planet. Space Sci.*, 30, 755, doi: [10.1016/0032-0633\(82\)90108-8](https://doi.org/10.1016/0032-0633(82)90108-8)
- . 1999, *Nature*, 400, 32, doi: [10.1038/21811](https://doi.org/10.1038/21811)
- Swain, M. R., Estrela, R., Sotin, C., Roudier, G. M., & Zellem, R. T. 2019, *ApJ*, 881, 117, doi: [10.3847/1538-4357/ab2714](https://doi.org/10.3847/1538-4357/ab2714)
- Tutukov, A. V. 1991, *AZh*, 68, 837
- Wahl, S. M., Hubbard, W. B., Militzer, B., et al. 2017, *Geophys. Res. Lett.*, 44, 4649, doi: [10.1002/2017GL073160](https://doi.org/10.1002/2017GL073160)
- Watson, A. J., Donahue, T. M., & Walker, J. C. G. 1981, *Icarus*, 48, 150, doi: [10.1016/0019-1035\(81\)90101-9](https://doi.org/10.1016/0019-1035(81)90101-9)
- Zeng, L., & Sasselov, D. 2013, *PASP*, 125, 227, doi: [10.1086/669163](https://doi.org/10.1086/669163)
- Zeng, L., Sasselov, D. D., & Jacobsen, S. B. 2016, *ApJ*, 819, 127, doi: [10.3847/0004-637X/819/2/127](https://doi.org/10.3847/0004-637X/819/2/127)
- Zeng, L., Jacobsen, S. B., Sasselov, D. D., et al. 2018, in *AGU Fall Meeting Abstracts*, Vol. 2018, P53C–2985

APPENDIX

A. EXTRA INFORMATION ON THE XUV FLUX

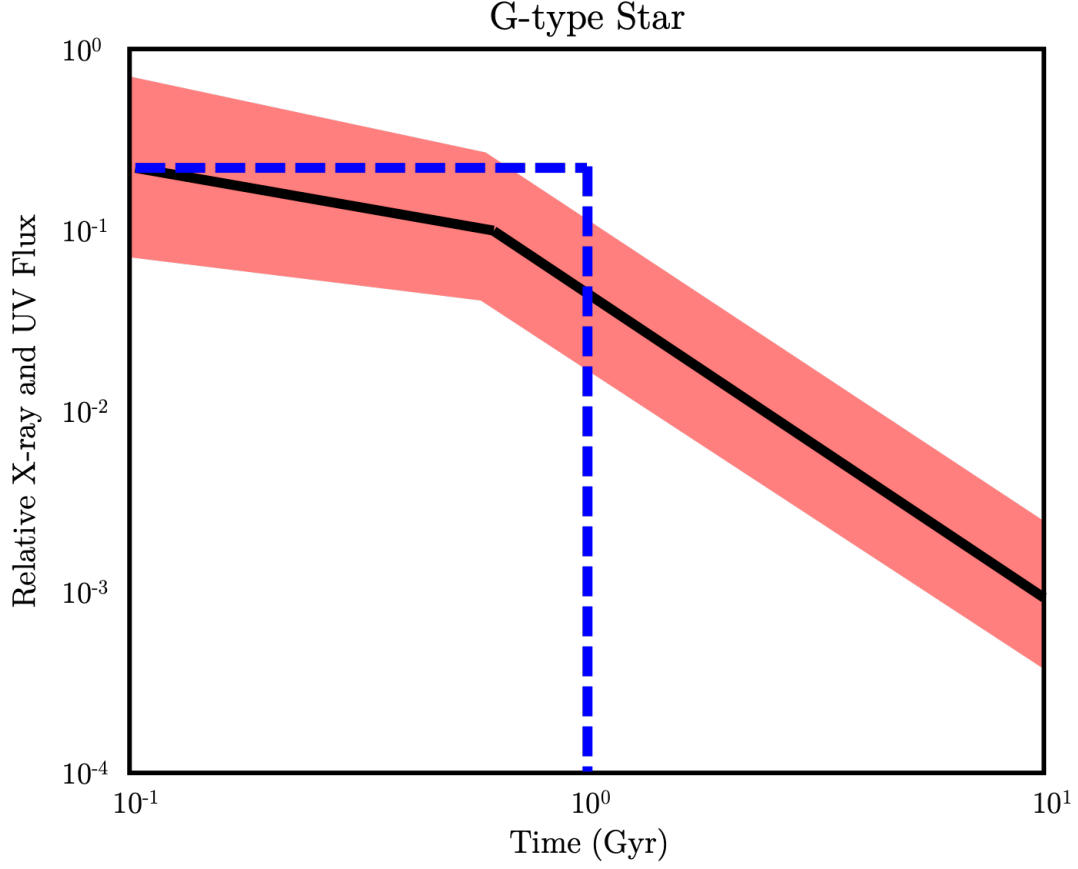


Figure 14. The relative XUV flux of G-type stars. The red shaded region marks the measurements from [Penz et al. \(2008\)](#) and [Sanz-Forcada et al. \(2011\)](#). The black line is the average measured XUV flux. The blue dashed line shows the step function we adopted in our model.

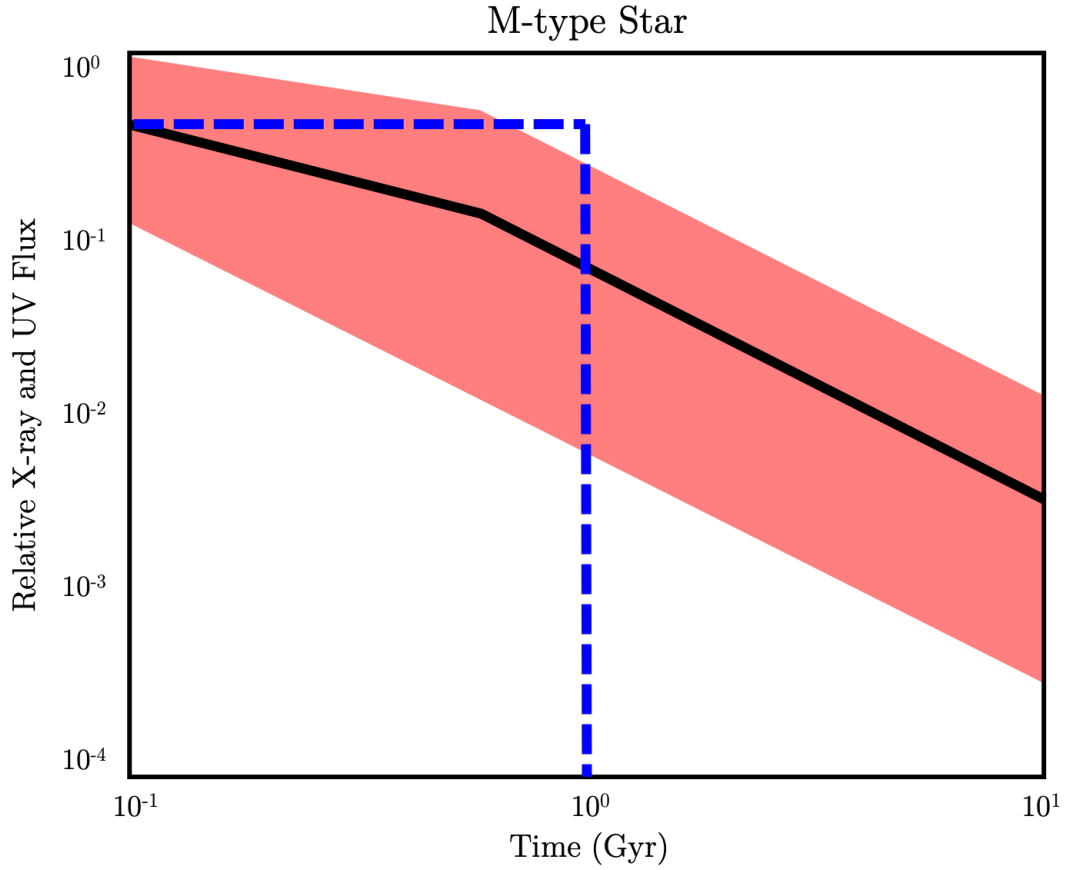


Figure 15. The relative XUV flux of M-type stars. The red shaded region marks the measurements from [Penz & Micela \(2008\)](#) and [Sanz-Forcada et al. \(2011\)](#). The black line is the average measured XUV flux. The blue dashed line shows the step function we adopted in our model.